ACS APPLIED MATERIALS & INTERFACES

www.acsami.org

Research Article

One-pot Synthesis of Metal-coordinated Covalent Organic Frameworks for Enhanced CO_2 Photoreduction

Hongbo Xue, Congcong Yin, Sen Xiong, Jingying Yang,* and Yong Wang*

Cite This: *ACS Appl. Mater. Interfaces* 2022, 14, 49672−49679

Read Online

ACCESS | Metrics & More | Article Recommendations | Supporting Information

ABSTRACT: Solar energy-driven reduction of CO_2 into fuels with H_2O as a sacrificial agent is a challenging but desirable subject in photosynthesis. Covalent organic frameworks (COFs) are considered promising candidates for this subject because of their designable structures and functions. The coordination of transition metal ions into COFs is a feasible way to boost the photocatalytic activity. However, postsynthetic modification of COFs with metal ions often leads to a significant decrease in crystallinity and the specific surface area. Herein, we develop a one-pot synthesis of metal-coordinated (nonnoble metal) COFs with high crystallinity. HB-TAPT + Co with ordered and segregated D−A arrays is synthesized by combining 2,4,6-tris(4-aminophenyl)-1,3,5-triazine (TAPT, a strong electron-acceptor) with 2-hydroxy-1,3,5-benzenetricarbaldehyde (HB)-loaded Co^{2+} (a strong electron-donor). The CO production when using HB-TAPT + Co under visible light irradiation for 4 h is 78.4 μmol g^{-1}, which is 3.2 times that of HB-TAPT + Co synthesized by the postsynthetic modification method and 2.65 times that of HB-TAPT without the metal ions. HB-TAPT + Co also has good recycling stability in photocatalytic CO_2 reduction. Additionally, experimental results have demonstrated that the crystallinities of these metal-coordinated materials contribute greatly to the conversion of CO_2 in the photoreaction with H_2O. This work provides a new protocol for improving the CO_2 photoreduction performance by coordinating metal ions to COFs while maintaining the original crystallinity through a one-pot synthesis method.

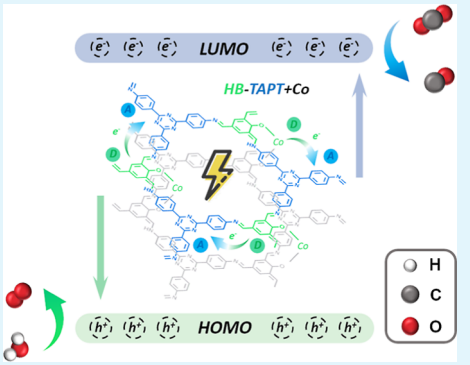

KEYWORDS: *covalent organic frameworks, photocatalysts, CO_2 photoreduction, one-pot synthesis method, carbon cycles*

1. INTRODUCTION

Fossil fuels, as the main energy source and the culprit of greenhouse gases, have caused a series of environmental problems.[1] Converting CO_2 into renewable energy or chemicals not only solves the urgent development problem but also creates additional economic value, thus gaining extensive attention.[2] CO_2 is highly symmetrical in the molecular structure and relatively stable in chemistry.[3,4] Many feasible and effective methods have been proposed for CO_2 reduction, for instance, thermocatalysis[5] and electrocatalysis,[6] but some imperfection points, such as high energy consumption and serious secondary pollution,[7,8] still demand prompt solutions. Light-driven CO_2 reduction to fuels and chemicals has been demonstrated as a promising strategy to overcome the levels of CO_2 in the atmosphere and simultaneously enrich the energy supply. Various molecules and semiconductor-based photocatalysts have been reported for CO_2 reduction.[9−12] However, there are still many challenges, mainly the severe photocorrosion rising from the recombination of the photogenerated electrons and holes or inadequate adsorption and activation capabilities of CO_2 on the semiconductor surface.[13] Therefore, it is highly important to develop efficient and robust catalyst systems with molecular-level structure design for improving the CO_2 reduction performance.

Covalent organic frameworks (COFs) are crystalline organic porous materials completely constructed by covalent bonding of organic monomers.[14,15] COFs with tunable structures and functions can be designed for CO_2 selective reduction through modular synthesis and structural diversity. The inerratic arrangement of electron donors (D) and electron acceptors (A) enhances photoelectron directional migration and reduces the recombination with holes, thus significantly promoting the photocatalytic performance.[16−18] However, the donor and acceptor moieties prefer to stack on one another rather than segregate to form bicontinuous alignments, and charge carriers are readily trapped and annihilated in the disordered structure.[19] Benefiting from the alternate construction (planar) and the regular $\pi-\pi$ stacking (interplanar), 2D COFs are suggested as promising candidates for solving this problem. The extensive π-delocalization in the extended conjugated plan structure benefits light harvesting, and $\pi-\pi$ stacking interactions would enhance

Received: July 12, 2022
Accepted: October 18, 2022
Published: October 31, 2022

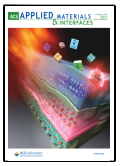

the transport and transfer of charge carriers along the planes and stacking directions. Additionally, the coordination of transition metal ions into 2D COFs is an efficient way to boost the photocatalytic activity. This can not only activate CO_2 molecules but also improve the transfer of photogenerated electrons from the host to the metal sites. Recently, a few metal ion-coordinated COF photocatalysts through postsynthetic modification (PSM) have been explored for the visible-light-driven reduction of CO_2.[20] Ye's group added single-atom MoN_3 into the COF to prepare Mo−COF materials.[21] Wang's group designed a nickel-modified COF (H−COF−Ni), which generated 5694 μmol g^{-1} of CO with a selectivity of up to 96%.[22] Lan's group recently presented a versatile strategy for uniformly dispersed polyoxometalates in COFs by a covalent linkage, which exhibited outstanding catalytic activity in photosynthesis.[23] Nonetheless, these systems require photosensitizers and electron sacrificial agents or cocatalysts, which increase the cost of reaction systems. Besides this problem, the PSM method may lead to the collapse of the structure, causing the low reduction efficiency.[24] Therefore, it is pivotal to establish a platform for metal-coordinated COF photocatalytic systems in an easy-to-do, economical method, which also helps in further understanding the photocatalytic reaction pathways.

In this work, we designed a one-pot synthetic method for constructing metal ion-coordinated COFs for photocatalytic CO_2 reduction in visible light. This one-pot method vastly simplified the synthesis procedure and, more importantly, kept the original crystallinity of COFs after introducing non-noble metal ions. The combination of the amine monomers (strong electron-accepting ability) with the aldehyde monomers coordinated with Co^{2+} (strong electron-donating ability) would offer a 2D COFs (HB-TAPT + Co). This 2D COFs photocatalyst having a D−A heterojunction structure is expected to provide a narrow band gap for extended spectral absorption. Furthermore, it would promote exciton splitting and charge transport. HB-TAPT + Co showed a considerable activity for visible-light-driven CO_2 reduction with H_2O. The exploration of metal ion-coordinated COFs prepared by the convenient and fast method of CO_2 reduction provides a molecular-level understanding of the inherent heterogeneous photocatalysis.

2. EXPERIMENTAL SECTION

2.1. Materials. Aldehyde monomers, 1,3,5-benzenetricarboxaldehyde (Tb, 98%), 2-hydroxy-1,3,5-benzenetricarbaldehyde (HB, 98%), and 2,4,6-triformylphloroglucinol (Tp, 98%) were purchased from Jilin Chinese Academy of Sciences-Yanshen Technology Co., Ltd. The amine monomer, 2,4,6-tris(4-aminophenyl)-1,3,5-triazine (TAPT, 98%), was bought from Heowns Biochem Technologies LLC. All the monomers were used without any purification. 1,3,5-Trimethylbenzene (97%), 1,4-dioxane (99%), acetic acid (Ac, 99%), cobalt acetate tetrahydrate ($Co(OAc)_2{\cdot}4H_2O$, 99.5%), nickel acetate tetrahydrate ($Ni(OAc)_2{\cdot}4H_2O$, 99.9%), zinc acetate dihydrate ($Zn(OAc)_2{\cdot}2H_2O$, 99%), and sodium sulfate (Na_2SO_4, 99%) were supplied by Shanghai Aladdin Biochemical Technology Co., Ltd. Conducting glass (fluoride tin oxide, FTO) was obtained from (Crystalgen Ningbo Biotech Ltd.). Nafion 117 (5%) was obtained from Sigma-Aldrich. Deionized water (H_2O) and carbon dioxide (CO_2, 99.9%) were purchased from local suppliers.

2.2. Synthesis of Photocatalysts. *2.2.1. One-pot Synthesis of HB-TAPT + Co.* A pyrex tube (o.d. × i.d. = 10 × 8 mm^2 and length 25 cm) was charged with HB (0.15 mmol, 27 mg), TAPT (0.15 mmol, 53 mg), $Co(OAc)_2{\cdot}4H_2O$ (10 mg), 1,3,5-trimethylbenzene (0.6 mL), 1,4-dioxane (3.0 mL), and 3 M acetic acid (0.6 mL). The mixture was treated by ultrasonication for 10 min to obtain a well-dispersed solution. After three freeze−pump−thaw cycles, the tube was vacuumed and sealed, and the reaction mixture was heated at 120 °C for three days. The dark red precipitate was isolated by filtration and washed with acetone (100 mL), H_2O (100 mL), and ethanol (200 mL). The product was dried under a vacuum at 120 °C for 12 h to yield HB-TAPT + Co (80 mg, 89%).

2.2.2. One-pot Synthesis of HB-TAPT + Ni and HB-TAPT + Zn. HB-TAPT + Ni and HB-TAPT + Zn were synthesized following the same procedures as that of HB-TAPT + Co, except that $Co(OAc)_2{\cdot}4H_2O$ (10 mg) was replaced by $Ni(OAc)_2{\cdot}4H_2O$ (10 mg) and $Zn(OAc)_2{\cdot}2H_2O$ (10 mg), respectively. Both HB-TAPT + Ni and HB-TAPT + Zn were dark red powders, and their yields were 83% (75 mg) and 87% (78 mg), respectively.

2.2.3. One-pot Synthesis of Tb-TAPT + Co and Tp-TAPT + Co. Tb-TAPT + Co and Tp-TAPT + Co were synthesized following the same procedures as that of HB-TAPT + Co, except that HB (0.15 mmol, 27 mg) was replaced by Tb (0.15 mmol, 24 mg) or Tp (0.15 mmol, 32 mg). Tb-TAPT + Co and Tp-TAPT + Co were afforded as yellow (65 mg, 75%) and orange powders (86 mg, 90%), respectively.

2.2.4. Synthesis of HB-TAPT, Tb-TAPT and Tp-TAPT. The synthesis procedure was the same as that of HB-TAPT + Co, but no metal ions were used. The resulting precipitates were collected as dark red, yellow, and orange powders to yield HB-TAPT (72 mg, 90%), Tb-TAPT (60 mg, 78%), and Tp-TAPT (74 mg, 87%), respectively.

2.2.5. Synthesis of HB-TAPT + Co with the PSM method. To a 100 mL round-bottom flask, 30 mg of HB-TAPT and 750 mg of $Co(OAc)_2{\cdot}4H_2O$ were added in a solvent of 50 mL of H_2O. The mixture was stirred for three days at the refluxing temperature. The precipitate was filtered, washed with deionized water (200 mL) and anhydrous ethanol (200 mL) for several times, and dried under a vacuum at 120 °C for 12 h to afford HB-TAPT + Co (26 mg, 87%) as a dark red solid.

2.3. Characterization. The Fourier transform infrared spectroscopy (FTIR, Thermo Fisher Scientific Nicolet 8700) and ^{13}C cross-polarization magic-angle-spinning solid-state NMR spectroscopy (CP-MAS, Bruker AVANCE III 400) were applied to characterize the chemical composition of monomers and COFs. Powder X-ray diffraction (PXRD, Rigaku SmartLab) was used to reveal the crystallinities of COFs. The specific surface areas of different photocatalysts were characterized by the multistation physical adsorption apparatus (ASAP 2460), and the pore size distributions were analyzed by the nonlocal density functional theory. The morphologies of photocatalysts were observed by an S-4800 field-emission scanning electron microscope (Hitachi) operating at 5 kV and transmission electron microscopy (TEM, FEI Talos F200X). Before field-emission scanning electron microscopy characterization, samples were coated with a layer of platinum using an ion sputter (Hitachi, MC1000) to enhance the conductivity. Elemental compositions of samples were analyzed by energy dispersive X-ray spectroscopy (EDS, Thermo Fisher Scientific SuperX G2), X-ray photoelectron spectroscopy (XPS, Thermo Fisher Scientific 250Xi), and inductively coupled plasma atomic emission spectrometry (ICP, Agilent 725).

An UV-3600 diffuse reflectance spectrophotometer (DRS, Shimazu) was used to characterize the energy gaps and absorbance edges of photocatalysts in a wavelength from 300 to 700 nm. The electrochemical property of COFs was analyzed by a CHI660E electrochemical workstation (Shanghai Chenhua). Samples (2 mg) were dispersed in ethanol (1 mL) along with 100 μL of Nafion 117, followed by an ultrasonication treatment to ensure that all samples were well dispersed. 200 μL of the dispersion was dropped on the conducting glass with a size of 10 mm × 30 mm, followed by air-drying. During tests, the conducting glasses coated with samples served as the working electrode. Pt was used as the counter electrode and Ag/AgCl was used as the reference electrode. Conducting bands and the impedances of COFs were analyzed by the Mott−Schottky (M−S) test and electrochemical impedance spectroscopy (EIS) using Na_2SO_4 solutions (30 mL, 0.5 M, pH = 7). In the photocurrent response tests, after illumination for 10 s by the xenon lamp (100 mW/cm^2), samples were placed in darkness for 10 s to record each measurement, which was repeated ten times.

https://doi.org/10.1021/acsami.2c12303
ACS Appl. Mater. Interfaces 2022, 14, 49672−49679

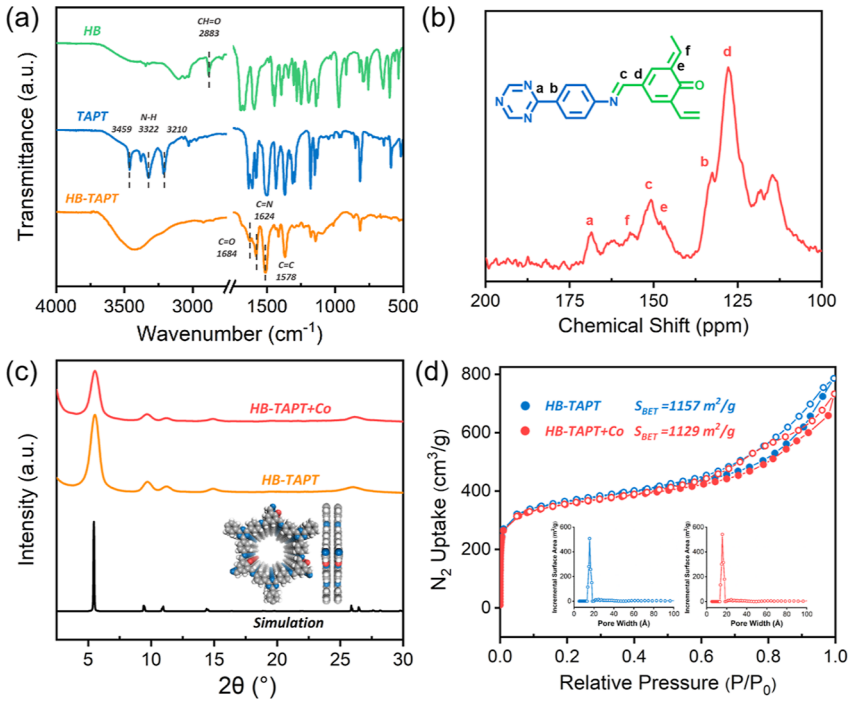

Figure 1. (a) FTIR spectra of HB, TAPT, and HB-TAPT; (b) solid-state ^{13}C NMR spectrum of HB-TAPT; (c) XRD patterns of HB-TAPT and HB-TAPT + Co (inset shows top views and side views of the space-filling models of HB-TAPT); and (d) nitrogen adsorption−desorption isotherms of HB-TAPT and HB-TAPT + Co (inset shows the pore size distributions).

2.4. Photocatalytic Reduction of CO_2 Tests. The photocatalytic test was conducted with the xenon lamp (400 mW/cm^2) in a top-illuminated quartz reactor (150 mL) at room temperature. First, 10 mg of samples and 50 mL of H_2O were added into the reactor and ultrasonicated for 15 min to obtain a complete dispersion solution. Prior to illumination, the reactor was thoroughly purged with CO_2 to remove air from the inside of the reactor. Then, the reactor was sealed and stirred magnetically at 500 rpm under the irradiation of a xenon lamp. During irradiation, samples (1 mL) were taken from the reactor every hour for the next 4 h and analyzed by a flame ionization detector and a thermal conductivity detector in gas chromatography (GC, Panna A91Plus). The durability and reusability tests were performed in the same way as mentioned above, but for seven times. After each test, the photocatalysts were recovered by centrifugation and dried at 120 °C in a vacuum for 12 h.

3. RESULTS AND DISCUSSION

3.1. Characterization. The chemical structures for all COFs are provided in Figure S1.

FTIR and solid-state ^{13}C NMR spectra were recorded to confirm the formation of imine bonds in HB-TAPT. Stretching vibrations of N−H (3459, 3322, and 3210 cm^{-1}) are shown in the spectrum of TAPT, and the strong stretching vibration of CH═O (2883 cm^{-1}) is presented in the spectrum of HB (Figure 1a).[25,26] After the Schiff-base condensation reaction, the CH═O peak of HB and the N−H peak of TAPT both disappear, and peaks of C═N (1624 cm^{-1}) and C═C (1578 cm^{-1}) are assigned to the newly formed HB-TAPT. The complete consumption of HB and the generation of the new characteristic peak (C═O, 1684 cm^{-1}) prove the keto−enol tautomerism, which makes the structure more stable. In the solid-state ^{13}C NMR spectrum of HB-TAPT (Figure 1b), the peak at 151 ppm is assigned to imine (C═N) carbon atoms, evidencing the formation of HB-TAPT. The resonance at ∼157 and 148 ppm are assigned to C═C, proving the formation of β-ketoenamine.

The crystal structures of HB-TAPT and HB-TAPT + Co were examined through PXRD with structural simulations. As shown in Figure 1c, HB-TAPT has a strong peak at 5.5°, corresponding to the (010) facet, which is consistent with the simulation, indicative of the highly crystalline nature. The characteristic peak at 25.9° is assigned to the (001) plane, which indicates a regular $\pi-\pi$ stacking structure of HB-TAPT.[27] This structure can migrate photo-generated electrons, and thus enhance the photocatalytic efficiency.[28] The experimental PXRD patterns match well with the simulated patterns obtained using the eclipsed stacking model. To find out the unit cell parameters, Pawley refinements were done for HB-TAPT, and the corresponding unit cell parameters are a = 18.82 Å, b = 18.38 Å, and c = 3.45 Å; $\alpha = \beta = \gamma = 90°$. The calculated PXRD pattern of HB-TAPT matches the experimental profile in peak positions and relative intensities well, with the factor of weighted profile (R_{wp}) of 7.17% and profile residual (R_p) of 5.42%. Note that, no additional peaks can be observed in the PXRD pattern of HB-TAPT + Co (Figure 1c), suggesting the successful reservation of the crystalline structure after Co^{2+} coordination.

The specific surface areas and pore size distributions of HB-TAPT and HB-TAPT + Co were analyzed by nitrogen adsorption−desorption isotherms. As shown in Figure 1d, trends of adsorption and desorption curves of HB-TAPT and HB-TAPT + Co are essentially the same. The rapid growth of the adsorption capacity of N_2 exhibited type I isotherms with a sharp increase at low relative pressures, indicating regular internal microporous structures. The specific surface areas of HB-TAPT and HB-TAPT + Co were calculated to be 1157 and 1129 m^2/g, respectively. The large specific surface area and the microporous structure are conducive to the adsorption of CO_2, which may improve the photocatalytic reduction efficiency. The relatively similar specific surface areas also prove that loading metal ions do not destroy the inherent microporous structure of HB-TAPT. In addition, the pore size distribution analysis gave

https://doi.org/10.1021/acsami.2c12303
ACS Appl. Mater. Interfaces 2022, 14, 49672−49679

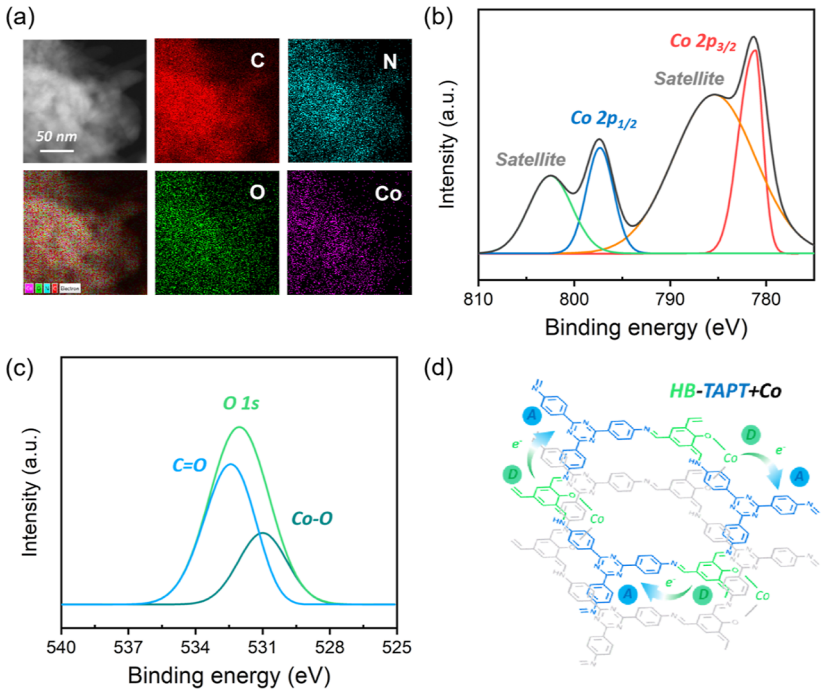

Figure 2. (a) EDS mapping, (b) Co 2p and (c) O 1s XPS spectra, and (d) structure diagram of HB-TAPT + Co.

rise to narrow pore size distributions of around 1.5 nm, which is consistent with that of the simulation network.

SEM and TEM were used to characterize the surface morphologies of HB-TAPT and HB-TAPT + Co. As shown in Figure S2, morphologies of both HB-TAPT and HB-TAPT + Co are clusters formed by the accumulation of nanoparticles. The morphologies were almost unchanged after coordination with Co^{2+}. By higher resolution TEM tests (Figure S3), both HB-TAPT and HB-TAPT + Co nanoparticles are rod-shaped. The COF particulates are rugged and fluffy, which are conducive to the gas adsorption and the photocatalytic CO_2 reduction.

Furthermore, EDS elemental mapping shows the homogeneous C, N, O, and Co atomic distribution (Figure 2a), and reveals a 1.2 wt % Co^{2+} content in HB-TAPT + Co, which is consistent with the ICP (1.41 wt %) and XPS results. In the Co 2p XPS spectrum (Figure 2b), two main peaks with binding energies of 797.4 and 781.3 eV, and two satellite peaks (802.6 and 785.6 eV) can be detected. Based on the energy values, the Co atoms within the HB-TAPT + Co are assigned to be Co(II) cations.[29,30] The fine O 1s XPS spectrum (Figure 2c) of HB-TAPT + Co reveals the presence of Co−O bonds. To confirm coordination on Co^{2+} between O atoms in HB-TAPT + Co, XPS analyses on HB-TAPT + Co and HB-TAPT were performed. As shown in Figure S4, O 1s in HB-TAPT + Co appear at a higher (532.5 eV) binding energy compared to HB-TAPT. Therefore, we understand that Co^{2+} are anchored between $\pi-\pi$ conjugated nanosheets by forming chemical bonds with carbonyl groups of HB-TAPT (Figure 2d),[26] which are also evidenced by the relatively similar specific surface areas of HB-TAPT and HB-TAPT + Co.

As shown in Figure S3a,b, band gaps of HB-TAPT (1.93 eV) and HB-TAPT + Co (1.98 eV) were determined by DRS. The wider band gap of HB-TAPT + Co is due to the introduction of Co^{2+}. Because the metal ion is more electron deficient, the electron density distribution of O atoms in the COF would shift to Co^{2+}. This would decrease the binding energy in the COF, thus leading to a lower conduction band position. However, the position of the valence band (VB) is not affected, and consequently, the gap band width rises slightly. Compared with traditional photocatalysts (TiO_2, 3.20 eV), the improved absorption edge would improve the efficiency of natural light, which has a significant influence on the actual use. The flat band potential can be determined by the Mott−Schottky (M−S) analysis. As shown in the insets of Figure S3a,b, the flat band potentials of HB-TAPT and HB-TAPT + Co are −1.00 and −1.07 V (vs Ag/AgCl), respectively, and the conduction band potentials are −0.59 and −0.66 V (vs RHE), which are both more negative than that of reducing CO_2 to CO (−0.53 V vs RHE). Considering the band gaps of HB-TAPT and HB-TAPT + Co, the corresponding VB potentials are 1.34 and 1.32 V (vs RHE), respectively (Figure S6), higher than that of oxidizing H_2O to O_2 (0.81 V vs RHE), suggesting the possibility for the reduction of the adsorbed CO_2 to CO. Calculation details are presented in the Supporting Information Section S3. A possible mechanism for the photoreduction of CO_2 over HB-TAPT + Co is proposed. The introduction of Co^{2+} helps the generation of electron−hole pairs produced by the light illumination of HB-TAPT + Co. The donor−acceptor heterojunction in HB-TAPT + Co offers adequate HOMO−LUMO separation of the election−hole pairs and enhances the intramolecular charge transfer. The electrons may transfer to Co species to form active species. CO_2 is adsorbed into COFs and interacts with the photoreduced Co species. After that, the adsorbed CO_2 molecules are reduced to CO through a cascade of redox reactions. Moreover, the N atoms inside the triazine rings generate active sites by facilitating the polarizability of CO_2 by dipole−quadrupole interactions. This would stabilize the delocalization of negative charges that prolongs the lifetime of photogenerated electrons. Introducing cobalt species into HB-TAPT could harvest more visible-light photos and produce more photogenerated carries than pristine HB-TAPT, thus promoting the enhancement of photoconversion efficiency.

3.2. Photocatalytic CO_2 Reduction. The photocatalytic CO_2 reduction of HB-TAPT + Co was evaluated under 1 atm

https://doi.org/10.1021/acsami.2c12303
ACS Appl. Mater. Interfaces 2022, 14, 49672−49679

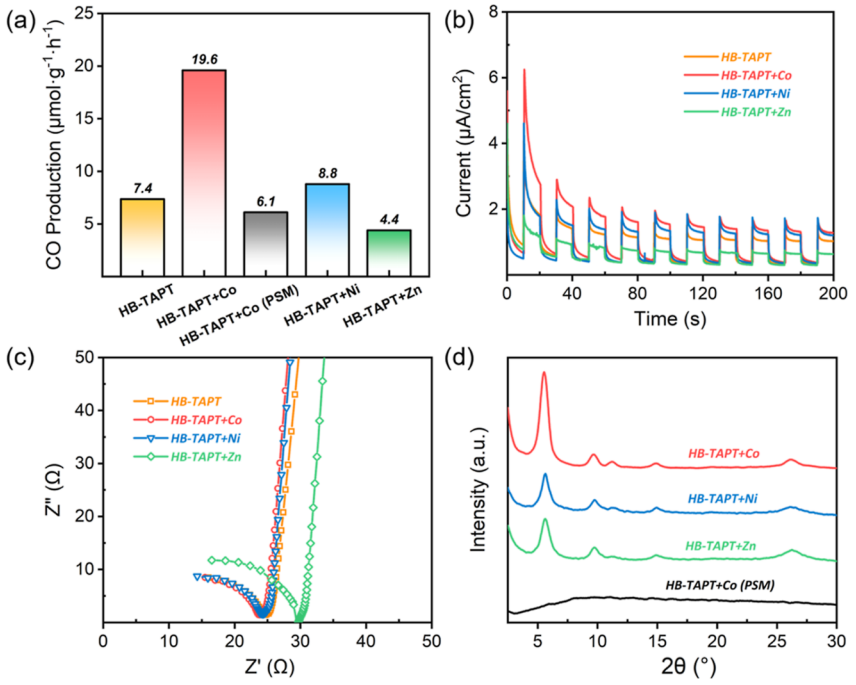

Figure 3. (a) Photocatalytic CO production, (b) transient photocurrent response curves, (c) EIS curves, and (d) XRD patterns of HB-TAPT, HB-TAPT + Co (one-pot), HB-TAPT + Co (PSM), HB-TAPT + Ni, and HB-TAPT + Zn.

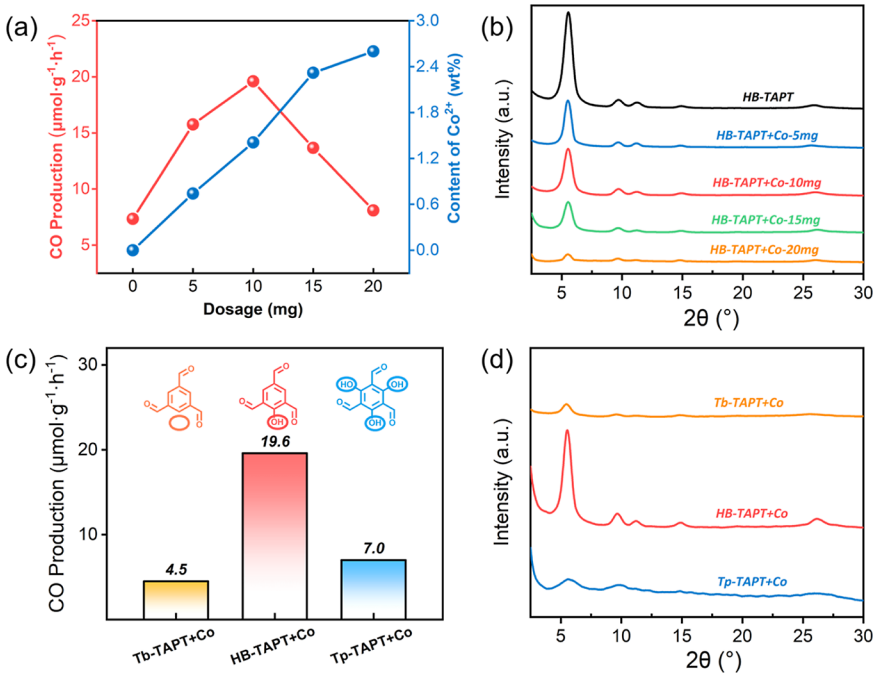

Figure 4. (a) CO production and Co^{2+} content, (b) XRD patterns of HB-TAPT with different dosages, (c) photocatalytic performances, and (d) XRD patterns of Tb, HB, and Tp-TAPT + Co.

CO_2 and visible light irradiation by a xenon lamp. As shown in Figure 3a, the photocatalytic CO production is only 29.6 μmol g^{-1} in 4 h if there is only the amine monomer TAPT as the strong electron acceptor in HB-TAPT without metal ions as electron donors. When Co^{2+} was introduced into the photocatalytic system, the activity is significantly enhanced. The evolution amount of CO was increased to 78.4 μmol g^{-1} in 4 h, which was 2.65 times that of HB-TAPT. The oxygen yield is 39.8 μmol g^{-1} in 4 h, which is consistent with the trend of the yield of CO produced by the photocatalysis. Coordination with metal ions greatly enhances the electron donating ability of HB by forming an intense electron donor−acceptor structure in COFs with the strong electron-donor, TAPT. Moreover, due to the alternate arrangement of aldehyde and amine monomers, as well as the stacking property of COF layers, the ordered and segregated donor−acceptor alignments are formed. The specific D−A structure is conductive to the directional migration of photoelectrons, reducing the recombination with holes.

A series of control experiments were performed to discern the roles of HB-TAPT + Co in CO_2 reduction. When the CO_2

https://doi.org/10.1021/acsami.2c12303
ACS Appl. Mater. Interfaces 2022, 14, 49672−49679

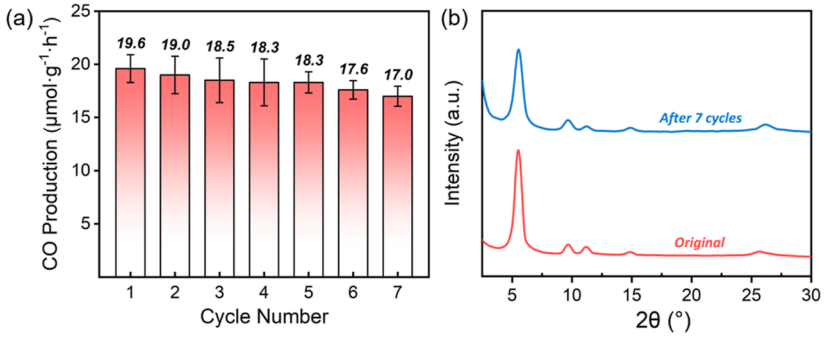

Figure 5. (a) Durability test results of HB-TAPT + Co and (b) XRD patterns of HB-TAPT + Co before and after the durability test.

reduction was conducted in the dark, the reaction system was completely inactive without producing any product, indicating that the system is a photosensitized process. HB-TAPT + Co (PSM) was also synthesized by the PSM method to compare with that by the one-pot method.[22] The photocatalytic CO production by HB-TAPT + Co (PSM) was only 6.1 μmol g^{-1} h^{-1}, even weaker than that of HB-TAPT without metal ion-loading. The PXRD spectrum has revealed that the crystal structure of HB-TAPT was collapsed during the PSM process. The characteristic peaks at 5.5 and 25.9° disappeared (Figure 3b), indicating that the crystallinity of HB-TAPT was completely destroyed, further revealing that the CO_2 conversion depends on the crystallinities of COFs.

Effects of different metal ions on the photocatalytic efficiency were also investigated. By adding the same mass (10 mg) of metal ions, Co^{2+}, Ni^{2+}, and Zn^{2+} are firmly anchored to HB-TAPT. According to ICP results, the contents of Co^{2+}, Ni^{2+}, and Zn^{2+} are 1.41, 2.14, and 0.97%, respectively. As shown in Figure 3a, the CO production by HB-TAPT + Co is 19.6 μmol g^{-1} h^{-1}, much better than that by HB-TAPT + Ni (8.8 μmol g^{-1} h^{-1}) and HB-TAPT + Zn (4.4 μmol g^{-1} h^{-1}). Co^{2+} prominently enhances the photocatalytic efficiency of HB-TAPT, while the photocatalytic performance was only slightly improved after HB-TAPT coordination with Ni^{2+}. In contrast, the introduction of Zn^{2+} reduced the CO production of HB-TAPT. The reasons can be analyzed from the following aspects. As shown in Figure 3b, the transient photocurrent response curve of HB-TAPT + Co is higher than those of others, indicating the superior charge separation efficiency, which is consistent with the actual CO production. Dynamic characteristics of charge transfer of photocatalysts were investigated by EIS, as shown in Figure 3c. HB-TAPT + Zn had a larger Nyquist arc radius than the others, which indicates that HB-TAPT + Zn has higher resistance values and lower electron transfer and carrier separation efficiency. At last, we check the crystallinities of all the samples. After introducing metal ions, the crystallinity of HB-TAPT + Co is much better than those of HB-TAPT + Ni and Zn (Figure 3d), revealing the reason for the best photocatalytic performance. The higher crystallinity means more ordered D−A arrays, which are beneficial for preventing photogenerated electron−hole recombination and minimizing charge trapping at defect sites.[28,31] Therefore, the high crystallinity is the key reason leading to the satisfactory performance of HB-TAPT + Co.

In order to explore the optimal ratio of metal ions to HB-TAPT, different masses of $Co(OAc)_2{\cdot}4H_2O$ were used in the synthesis. As shown in Figure 4a, with the dosage rising from 0 to 20 mg, the photocatalytic CO production increased first and decreased later. When 10 mg dosage was applied (Co^{2+} content is 1.41%), the CO production reached its peak. The relationship between the dosage and the Co^{2+} content was characterized by ICP, which was proven to be an approximately linear proportion.

To find out the reason for the variation of photocatalytic properties, crystallinities of catalysts were characterized by PXRD (Figure 4b). With the increasing Co^{2+} content, the inherent crystallinity of HB-TAPT gradually declined until its complete loss. The proper dosage of $Co(OAc)_2{\cdot}4H_2O$ effectively promoted the photocatalytic performance of HB-TAPT, but excessive dosage would decrease the crystallinity of photocatalysts. Poor crystallization structures would accelerate the recombination of photoelectrons and holes, shorten the lifetime of charge carriers, and reduce the photocatalytic efficiency.

The aldehyde monomer HB contains only one hydroxyl group, which would be converted to the carbonyl group in COFs via keto−enol tautomerism, providing bonding sites for Co^{2+}. With more hydroxyl groups in the aldehyde structure, more metal ions are expected to coordinate with the aldehyde monomers. To investigate the influence of the number of bonding sites in photocatalytic CO_2 reduction, aldehyde monomers (Tb, HB, and Tp) with different numbers of hydroxyl groups (0, 1, and 3) were reacted with the same amine monomer TAPT to synthesize a series of photocatalysts. As expected, the photocatalytic efficiency of Tb-TAPT + Co without the carbonyl group in the chemical structure was not promoted (Figure 4c) because of the absence of efficient electron donors. For Tp-TAPT + Co, excessive active sites may lead to the chaotic configuration of Co^{2+}, disrupting the directional migration of photoelectrons, which inhibits the improvement of photocatalytic abilities. Meanwhile, the crystallinity of Tp-TAPT + Co prepared by the one-pot synthesis method is obviously weaker than that of HB-TAPT + Co (Figure 4d). The random distribution of donors and acceptors, and the relatively low crystallinity of Tp-TAPT + Co are both attributed to its mediocre performance.

In order to avoid secondary pollution and the consumption of chemicals, pure water was used as the only reducing agent in the photocatalytic process without any sacrificial agents. The performance of photocatalytic CO_2 reduction by COFs and other materials at the same condition is shown in Table S1. Compared with the competition, organic photocatalysts, both the CO production and the stability of HB-TAPT + Co are better. Compared with the COF-based photocatalysts with noble metals, HB-TAPT + Co is low cost, easy to prepare, and well behaved.

3.3. Durability and Reusability. Seven cycles of photocatalytic CO_2 reduction experiments (4 h) were conducted to test the reusability of HB-TAPT + Co. As shown in Figure 5a,

https://doi.org/10.1021/acsami.2c12303
ACS Appl. Mater. Interfaces 2022, 14, 49672−49679

HB-TAPT + Co shows excellent durability and stability, and the photocatalytic performance of the 7th cycle is 17.0 μmol g^{-1} h^{-1}, which is about 90% of the 1st cycle. The high crystallinity of HB-TAPT + Co was retained after seven cycles (Figure 5b), indicating that the sample was not corroded by the long illumination time. The FTIR spectrum of the recovered HB-TAPT + Co does not show any major changes (Figure S7) when compared with that of the as-prepared samples.

4. CONCLUSIONS

In this work, we report the design of HB-TAPT + Co as a synergistic catalyst, which possesses a suitable energy band level to reduce CO_2 to CO with H_2O as the electron donor, without using any additional photosensitizers or electron sacrificial agents. Co^{2+} ions are successfully anchored in HB-TAPT by a convenient one-pot method. In order to explore the optimal photocatalytic performance, the reduction efficiencies of catalysts with different doping methods, types, and contents of metal ions are investigated. Thanks to the ordered and segregated D−A arrays formed in HB-TAPT + Co prepared by our one-pot method, the recombination of photoelectrons with holes is reduced, and the efficiency of photocatalytic CO_2 reduction is significantly promoted. HB-TAPT + Co (one-pot) achieves a high photocatalytic CO production of 78.4 μmol g^{-1} in 4 h. In addition, the photocatalyst is recoverable and reusable after the reaction without major change in the catalytic activities. We develop a more straightforward protocol for preparing the metal ion-coordinated COFs photocatalysts, which could maintain the high crystallinity during the whole reaction. Moreover, it has been confirmed that besides the addition of Co^{2+} providing more active sites for stable CO_2 molecule adsorption and photocatalysis, the number of hydroxyl groups in COFs also has played a significant role due to its effect on the crystallinity. This will help us understand the structure−function relationship of heterogeneous photocatalysts and develop new COF-based photocatalytic systems for solar-to-chemical conversion.

■ ASSOCIATED CONTENT

Supporting Information

The Supporting Information is available free of charge at https://pubs.acs.org/doi/10.1021/acsami.2c12303.

SEM images; TEM images; energy band structures; photocatalytic performance comparison; and FTIR spectra (PDF)

Crystallographic data for HB-TAPT (CIF)

Crystallographic data for Triazine-Co (CIF)

■ AUTHOR INFORMATION

Corresponding Authors

Jingying Yang − *State Key Laboratory of Materials-Oriented Chemical Engineering, and College of Chemical Engineering, Nanjing Tech University, Nanjing 211816 Jiangsu, P. R. China*; orcid.org/0000-0002-2932-9542; Phone: +86-25-83172247; Email: jyyang@njtech.edu.cn; Fax: +86-25-83172292

Yong Wang − *State Key Laboratory of Materials-Oriented Chemical Engineering, and College of Chemical Engineering, Nanjing Tech University, Nanjing 211816 Jiangsu, P. R. China*; orcid.org/0000-0002-8653-514X; Email: yongwang@njtech.edu.cn

Authors

Hongbo Xue − *State Key Laboratory of Materials-Oriented Chemical Engineering, and College of Chemical Engineering, Nanjing Tech University, Nanjing 211816 Jiangsu, P. R. China*

Congcong Yin − *State Key Laboratory of Materials-Oriented Chemical Engineering, and College of Chemical Engineering, Nanjing Tech University, Nanjing 211816 Jiangsu, P. R. China*

Sen Xiong − *State Key Laboratory of Materials-Oriented Chemical Engineering, and College of Chemical Engineering, Nanjing Tech University, Nanjing 211816 Jiangsu, P. R. China*

Complete contact information is available at: https://pubs.acs.org/10.1021/acsami.2c12303

Notes

The authors declare no competing financial interest.

■ ACKNOWLEDGMENTS

We gratefully acknowledge financial support from the Jiangsu Natural Science Foundation (BK20190677) and the National Natural Science Foundation of China (21908096).

■ REFERENCES

(1) Albini, A.; Fagnoni, M. 1908: Giacomo Ciamician and the Concept of Green Chemistry. *ChemSusChem* **2008**, *1*, 63−66.

(2) Heindel, N. D.; Pfau, M. A. A Profitable Partnership: Giacomo Ciamician and Paul Silber. *J. Chem. Educ.* **1965**, *42*, 383−386.

(3) Chang, X.; Wang, T.; Gong, J. CO_2 Photo-Reduction: Insights into CO_2 Activation and Reaction on Surfaces of Photocatalysts. *Energy Environ. Sci.* **2016**, *9*, 2177−2196.

(4) Kim, W.; Edri, E.; Frei, H. Hierarchical Inorganic Assemblies for Artificial Photosynthesis. *Acc. Chem. Res.* **2016**, *49*, 1634−1645.

(5) Mehla, S.; Kandjani, A. E.; Babarao, R.; Lee, A. F.; Periasamy, S.; Wilson, K.; Ramakrishna, S.; Bhargava, S. K. Porous Crystalline Frameworks for Thermocatalytic CO_2 Reduction: an Emerging Paradigm. *Energy Environ. Sci.* **2021**, *14*, 320−352.

(6) Zhao, R. B.; Ding, P.; Wei, P. P.; Zhang, L. C.; Liu, Q.; Luo, Y. L.; Li, T. S.; Lu, S. Y.; Shi, X. F.; Gao, S. Y.; Asiri, A. M.; Wang, Z. M.; Sun, X. P. Recent Progress in Electrocatalytic Methanation of CO_2 at Ambient Conditions. *Adv. Funct. Mater.* **2021**, *31*, 2009449.

(7) Li, K.; Peng, B.; Peng, T. Recent Advances in Heterogeneous Photocatalytic CO_2 Conversion to Solar Fuels. *ACS Catal.* **2016**, *6*, 7485−7527.

(8) Li, Z.; Feng, J.; Yan, S.; Zou, Z. Solar Fuel Production: Strategies and New Opportunities with Nanostructures. *Nano Today* **2015**, *10*, 468−486.

(9) Zhang, W. H.; Mohamed, A. R.; Ong, W. J. Z-Scheme Photocatalytic Systems for Carbon Dioxide Reduction: Where Are We Now? *Angew. Chem., Int. Ed.* **2020**, *59*, 22894−22915.

(10) Gao, C.; Low, J. X.; Long, R.; Kong, T. T.; Zhu, J. F.; Xiong, Y. J. Heterogeneous Single-Atom Photocatalysts: Fundamentals and Applications. *Chem. Rev.* **2020**, *120*, 12175−12216.

(11) Ouyang, T.; Wang, H.-J.; Huang, H.-H.; Wang, J.-W.; Guo, S.; Liu, W.-J.; Zhong, D.-C.; Lu, T.-B. Dinuclear Metal Synergitic Catalysis Boosts Photochemical. CO_2-to-CO Conversion. *Angew. Chem., Int. Ed.* **2018**, *57*, 16480−16485.

(12) Yang, W.; Wang, H.-J.; Liu, R.-R.; Wang, J.-W.; Zhang, C.; Li, C.; Zhong, D.-C.; Lu, T.-B. Tailoring Crystal Facets of Metal-Organic Layers to Enhance Photocatalytic Activity for CO_2 Reduction. *Angew. Chem., Int. Ed.* **2021**, *60*, 409−414.

(13) Wagner, A.; Sahm, C. D.; Reisner, E. Towards Molecular Understanding of Local Chemical Environment Effects in Electro- and Photocatalytic CO_2 Reduction. *Nat. Catal.* **2020**, *3*, 775−786.

(14) Wang, G. B.; Li, S.; Yan, C. X.; Zhu, F. C.; Lin, Q. Q.; Xie, K. H.; Geng, Y.; Dong, Y. B. Covalent Organic Frameworks: Emerging High-Performance Platforms for Efficient Photocatalytic Applications. *J. Mater. Chem. A* **2020**, *8*, 6957−6983.
(15) Liang, R. R.; Jiang, S. Y.; A, A.; Zhao, X. Two-dimensional Covalent Organic Frameworks with Hierarchical Porosity. *Chem. Soc. Rev.* **2020**, *49*, 3920−3951.
(16) Shang, T. Y.; Lu, L. H.; Cao, Z.; Liu, Y.; He, W. M.; Yu, B. Recent Advances of 1,2,3,5-tetrakis(carbazol-9-yl)-4,6-dicyanobenzene (4CzIPN) in Photocatalytic Transformations. *Chem. Commun.* **2019**, *55*, 5408−5419.
(17) Windle, C. D.; Perutz, R. N. Advances in Molecular Photocatalytic and Electrocatalytic CO_2 Reduction. *Coord. Chem. Rev.* **2012**, *256*, 2562−2570.
(18) Zhang, M.; Chang, J.-N.; Chen, Y.; Lu, M.; Yu, T.-Y.; Jiang, C.; Li, S.-L.; Cai, Y.-P.; Lan, Y.-Q. Controllable Synthesis of COFs-Based Multicomponent Nanocomposites from Core-Shell to Yolk-Shell and Hollow-Sphere Structure for Artificial Photosynthesis. *Adv. Mater.* **2021**, *33*, 2105002.
(19) Feng, X.; Chen, L.; Honsho, Y.; Saengsawang, O.; Liu, L. L.; Wang, L.; Saeki, A.; Irle, S.; Seki, S.; Dong, Y. P.; Jiang, D. L. An Ambipolar Conducting Covalent Organic Framework with Self-Sorted and Periodic Electron Donor-Acceptor Ordering. *Adv. Mater.* **2012**, *24*, 3026−3031.
(20) Nguyen, H. L.; Alzamly, A. Covalent Organic Framworks as Emerging Platforms for CO_2 Photoreduction. *ACS Catal.* **2021**, *11*, 9809−9824.
(21) Kou, M.; Liu, W.; Wang, Y.; Huang, J.; et al. Photocatalytic CO2 Conversion over Single-Atom MoN2 sites of Covalent Organic Framwork. *Applied Catalysis B: Environmental* **2021**, *291*, 120146.
(22) Yang, S.; Sa, R.; Zhong, H.; Lv, H.; Yuan, D.; Wang, R. Microenvironments Enabled by Covalent Organic Framwork Linkages for Modulating Active Metal Species in Photocatalytic CO2 Reduction. *Adv. Funct. Mater.* **2022**, *32*, 2110694.
(23) Lu, M.; Zhang, M.; Liu, J.; Yu, T.-Y.; Chang, J.-N.; Shang, L.-J.; Li, S.-L.; Lan, Y.-Q. Confining and Highly Dispersing Single Poluxometalate Clusters in Covalent Organic Framworks by Covalent Linkages for CO_2 Photoreduction. *J. Am. Chem. Soc.* **2022**, *144*, 1861−1871.
(24) Lin, C. X.; Liu, X. L.; Yu, B. Q.; Han, C. Z.; Gong, L.; Wang, C. M.; Gao, Y.; Bian, Y. Z.; Jiang, J. Z. Rational Modification of Two-Dimensional Donor-Acceptor Covalent Organic Frameworks for Enhanced Visible Light Photocatalytic Activity. *ACS Appl. Mater. Interfaces* **2021**, *13*, 27041−27048.
(25) Karak, S.; Kumar, S.; Pachfule, P.; Banerjee, R. Porosity Prediction through Hydrogen Bonding in Covalent Organic Frameworks. *J. Am. Chem. Soc.* **2018**, *140*, 5138−5145.
(26) Wang, H.; Wang, H.; Wang, Z. W.; Tang, L.; Zeng, G. M.; Xu, P.; Chen, M.; Xiong, T.; Zhou, C. Y.; Li, X. Y.; Huang, D. N.; Zhu, Y.; Wang, Z. X.; Tang, J. W. Covalent organic framework photocatalysts: structures and applications. *Chem. Soc. Rev.* **2020**, *49*, 4135−4165.
(27) Lu, M.; Li, Q.; Liu, J.; Zhang, F. M.; Zhang, L.; Wang, J. L.; Kang, Z. H.; Lan, Y. Q. Installing Earth-Abundant Metal Active Centers to Covalent Organic Frameworks for Efficient Heterogeneous Photocatalytic CO_2 Reduction. *Appl. Catal., B* **2019**, *254*, 624−633.
(28) Auras, F.; Ascherl, L.; Hakimioun, A. H.; Margraf, J. T.; Hanusch, F. C.; Reuter, S.; Bessinger, D.; Döblinger, M.; Hettstedt, C.; Karaghiosoff, K.; Herbert, S.; Knochel, P.; Clark, T.; Bein, T. Synchronized Offset Stacking: A Concept for Growing Large-Domain and Highly Crystalline 2D Covalent Organic Frameworks. *J. Am. Chem. Soc.* **2016**, *138*, 16703−16710.
(29) Li, Q.; Zhou, J.; Liu, R.; Han, L. An amino-functionalized metal-organic framework nanosheet array as a battery-type electrode for an advanced supercapattery. *Dalton Trans.* **2019**, *48*, 17163−17168.
(30) Zhao, L.; Zheng, L.; Li, X.; Wang, H.; Lv, L.-P.; Chen, S.; Sun, W.; Wang, Y. Cobalt Coordinated Cyano Covalent-Organic Framework for High-Performance Potassium-Organic Batteries. *ACS Appl. Mater. Interfaces* **2021**, *13*, 48913−48922.
(31) Wang, X. Y.; Chen, L. J.; Chong, S. Y.; Little, M. A.; Wu, Y. Z.; Zhu, W. H.; Clowes, R.; Yan, Y.; Zwijnenburg, M. A.; Sprick, R. S.; Cooper, A. I. Sulfone-Containing Covalent Organic Frameworks for Photocatalytic Hydrogen Evolution from Water. *Nat. Chem.* **2018**, *10*, 1180−1189.

https://doi.org/10.1021/acsami.2c12303
ACS Appl. Mater. Interfaces 2022, 14, 49672−49679